Received: 21 May 2019 | Revised: 3 September 2019 | Accepted: 5 September 2019

DOI: 10.1002/mrm.28012

FULL PAPER

Magnetic Resonance in Medicine

Insights into tissue microstructure using a double diffusion encoding sequence on a clinical scanner: Validation and application to experimental tumor models

Gaëtan Duchêne[1] | Jorge Abarca-Quinones[1,2] | Isabelle Leclercq[1,2] | Thierry Duprez[1,2] | Frank Peeters[2]

[1]Université Catholique de Louvain, Brussels, Belgium

[2]Cliniques Universitaires Saint-Luc, Brussels, Belgium

Correspondence
Gaëtan Duchêne, Avenue Mounier 72/B1.72.06, Bruxelles 1200, Belgium.
Email: gaetan.duchene@uclouvain.be

Purpose: To present a double diffusion encoding MRI sequence on a clinical scanner to analyze micro-structure and micro-vasculature of tumors.

Methods: The sequence was tested on phantoms, asparaguses, and 2 tumors allografts in a rodent. Results were analyzed using an adapted VERDICT model to estimate microstructural parameters. The technical feasibility of the sequence on a 3T clinical system was assessed on a water phantom. The accuracy of cell size estimation was assessed on asparaguses by comparison with light microscopy. Cell size estimations were also validated when limiting relative angles of diffusion encodings to 0 and 180°. Sensitivities to restricted diffusion and incoherent flow from the vasculature were investigated in experimental tumor models. Values of microstructural parameters in viable and decaying tumor tissue were compared with those obtained from histological analysis.

Results: Measurements on the water phantom revealed no significant sequence artifacts and accurate apparent diffusion coefficient values within a 4% relative error. In asparaguses, quartiles and medians of pore size distributions typically deviated less than 6% from light microscopy regardless of whether the full or reduced set of relative angles was used. Signal analyses in tumors showed mixed effects of both blood flow and diffusion restriction. Microstructural parameter estimations in tumors were consistent with histology and allowed clear and histology-proven distinctions between decaying and viable tumor tissue.

Conclusions: Double diffusion encoding with clinical gradients and scan times allows characterization of restricted diffusion and micro-circulation flow in tumors. Our estimated microstructural parameters are promising for further investigations in assessing microstructural evolutions in tumors.

KEYWORDS

diffusion MRI, double diffusion encoding, microstructure, PGSE, tumors, validation

1 | INTRODUCTION

Diffusion MRI (dMRI) increasingly raises interest in clinical radiology,[1] particularly in oncology.[2] The main strength of dMRI is its sensitivity to the microstructure of tissues. The apparent diffusion coefficient (ADC)[3] reflects the water mobility in an image voxel. For instance, ADC in tumors is often interpreted in terms of the inverse of cellularity, where an increased cell density would lead to more restricted water diffusion and a decrease in ADC. However, this interpretation is controversial.[4] In practice, ADC is calculated the same way as for free, Gaussian diffusion. In the presence of biological restrictions to diffusion (like cell membranes) a reduced diffusion coefficient, therefore, termed *apparent*, is obtained. For this reason, the ADC is a global metric of which interpretation may be not straightforward as it contains convoluted effects of cell membranes, extracellular matrix, vascularization, cell nuclei, etc.

Microstructure modeling has emerged in dMRI as a way to disentangle effects of tissue components on diffusion measurements. In this approach, the MR signal is seen as the sum of several distinct signals produced by different compartments of tissues. The problem is, therefore, to find compartments' descriptors that produce the best fit of the MR signal. The earliest example is the bi-exponential model where the signal is modeled as the sum of 2 exponential MR signals,[5] each corresponding to Gaussian diffusion. In this analysis, descriptors are fractions of each compartment and their associated ADCs termed fast and slow for the higher and lower ADC values, respectively. Although improving the fit quality, biophysical foundations of the bi-exponential model remain unclear.[6,7]

To improve the link between diffusion measurements and the actual tissue morphology, some compartments may be modeled as restricted diffusion (RD) in a simple specific geometry (usually spherical or cylindrical) to represent intracellular diffusion while others may be modeled as Gaussian diffusion to represent extracellular diffusion. For instance, in Composite Hindered And Restricted ModEl of Diffusion (CHARMED), for studying white matter,[8] axons are represented as a cylindrical geometry while the extracellular matrix is represented as hindered diffusion, which is Gaussian diffusion but with an ADC whose value drops with increasing tortuosity between cells. Numerous multi-compartments models exist for the central nervous system[9-11] depending on the application.

When microvasculature is present within tissues, both diffusion and perfusion may have an impact on diffusion encoded signals. The most common framework is the intravoxel incoherent motion (IVIM) model[12] that can be used to separate diffusion in the parenchyma from diffusion and flow in the capillaries. Contributions of flow may be observed in 2 regimes depending on the diffusion time Δ.[13] In the ballistic regime, Δ is such that the flow does not experience directional changes during diffusion encoding. Conversely, when many directional changes occur during Δ the flow mimics a fast diffusion-like regime usually referred to as pseudo-diffusion. In this case, the vascular compartment can be modeled as Gaussian diffusion with a pseudo-ADC formed by the sum of the blood ADC and a high ADC that mimics the perfusion.[13]

In tumors, a popular model is Vascular, Extracellular and Restricted Diffusion for Cytometry in Tumors (VERDICT)[14] and models the MR signal with 3 compartments: the intracellular, extracellular and vascular environments. VERDICT has been shown to be sensitive to chemically induced apoptosis in xenografts[14] and has also been applied to differentiate normal and malignant tissues in human prostate cancer.[15] Intracellular diffusion is modeled as RD in impermeable spheres while Gaussian diffusion is used for the extracellular matrix. For the vascular compartment, early versions of VERDICT in xenografts proposed an anisotropic tensor of pseudo-diffusion.[14] In human prostate, the vasculature model is somewhat different from IVIM as it is represented by sticks (i.e., zero radius cylinders) in which fast diffusion occurs.[15]

Another important aspect of microstructure imaging is the MR pulse sequence. VERDICT uses a single diffusion encoding scheme which refers to a standard diffusion weighted sequence (i.e., using a single diffusion encoding gradient pair) but where several b-values are taken with both varying diffusion times and gradient areas (q-values).[14] The reason for using different Δ is to increase sensitivity to cell sizes as the relationship between Δ and the mean squared displacement of water molecules depends on the size of restricting geometries.[16] The effect of restricting geometry length on diffusion will be referred to as RD in the manuscript. Ultra-short diffusion times can be achieved with an oscillating gradient spin echo sequence. In tumors, oscillating gradient spin echo has been applied[17] with imaging microstructural parameters using limited spectrally edited diffusion (IMPULSED) to measure cell sizes and cellularity on a preclinical MR scanner. Double diffusion encoding (DDE) has also been proposed to quantify cell sizes.[18-28] In DDE, 2 diffusion encoding gradient pairs are successively applied with 2 different orientations, separated by a relative angle ψ. For adjacent gradient pairs (i.e., zero mixing time, t_m), molecular displacements during encodings are correlated, which confers a high sensitivity to RD. Besides RD, DDE has also been shown to be sensitive to ballistic flow occurring in the vascular network when using both 0 (parallel) and 180° (anti-parallel) relative angles[29] that are flow compensated and uncompensated, respectively.[30]

Implementation of a DDE sequence on a clinical scanner is challenging.[31] The available maximum gradient strength is typically limited to 40-80 mT/m and the scan time should be acceptable for patients. In this work, we present a pilot study of a DDE sequence implemented on a clinical scanner using different ψ and q-values for analyzing tumors' microstructure

with a VERDICT model adapted for ballistic flow. The first step of the study was to assess the sequence technical viability by measurements on a water phantom. Next, the potential of DDE to yield accurate cell size estimations was tested on asparaguses which feature simple morphology allowing straightforward cell size validation by light microscopy (LM). In this step, we also investigated if a parallel–anti-parallel (P-AP)[29] version of the sequence using only 0 and 180° relative angles would be sufficient for cell size estimations. For translation to tumors, a DDE protocol with P-AP measurements along 3 orthogonal directions is proposed. The sensitivity of our DDE protocol to both RD and ballistic flow in tumors was investigated. Finally, microstructural parameters estimated from DDE measurements in tumors were compared with histology. The results suggest that RD and vascularization sensitivities of DDE have the potential to monitor tumors' microstructural evolutions to treatment which we aim to investigate in the future.

2 | METHODS

2.1 | Imaged specimens

The first phantom is a 0°C water bottle whose diffusion coefficient is known to be 1.099 $\mu m^2/ms$.[32,33] It was used to ensure that parameter estimations were not biased by imperfections in our DDE sequence.

Five white asparaguses' stems were used as a biological phantom. The advantage of using asparaguses is that they naturally display well aligned impermeable cylinders whose radii can be easily assessed by LM. Indeed, the peripheral belt of the stem is composed of fibrous and thick-walled[34] cells. The epidermis is the outermost single layered arrangement of cells and directly surrounds the pro-epidermis (PE) that is typically formed by elongated cells that contains chloroplasts and provides structural support to the plant.[34-36] The purpose of imaging asparaguses is to check if our DDE sequence yields consistent cell sizes in the PE which offers a primary validation.

For analyses in tumors, 2 allografts were taken from a rhabdomyosarcoma model developed by the Laboratory of Experimental Radiobiology of the Katholiek Universiteit Leuven (Belgium).[37] They were implanted subcutaneously in each thigh of a 10-week-old male WAG/Rij rat (Charles River, Wilmington, MA). The animal was anesthetized with a ketamine (80 mg/kg)/xylazine (10 mg/kg) mixture during surgical procedures. Allografts volumes were approximately 1 mm^3 and grew during 14 days to reach approximately 9 and 7 cm^3 for the left and right thigh, respectively. During the MRI session, the rat was anesthetized with 1.5% isoflurane in 100% O_2. After MRI, tumors were extracted and the animal was killed by a lethal dose of the Ket/Xyl mixture. All manipulations on the animal were in accordance with our institutional ethical committee (project number: 2017/UCL/MD/018). In this rhabdomyosarcoma model, tumors' diameters typically increase by 50% in a few days.[38] In such rapidly growing tumors, ischemic necrosis is a common feature where massive cell proliferation leads to hypoxia by obstructing blood vessels, leading in turn to large areas of decaying tissue.[39]

2.2 | MRI

The DDE sequence was implemented on a 3T Achieva (PhilipsTM, Best, The Netherlands) scanner equipped with 80 mT/m gradients. The sequence is represented in Figure 1. It is a single shot double spin-echo echo-planar sequence with total echo time (TE) = TE1 + TE2. The 4 gray-filled gradients have the same area and are used for diffusion encoding. A dashed copy of the second gradient pair highlights that it may not have the same orientation than the first one. To avoid ambiguities, we refer to the diffusion encoding direction of the DDE sequence as the direction of the first gradient pair. The relative angle (ψ) defines the direction of the second gradient pair with respect to the first one in a given plane. Except for their orientations, the 2 gradient pairs are identical and adjacent, without any overlap, which fixes the mixing time to 1 gradient lobe duration ($t_m = \delta$). Crusher gradients are also shown. Their areas were optimized using measurements on a wrist coil phantom (small bottle with $CuSO_4$ solution) to suppress imaging artifacts. To minimize eddy-currents effects,

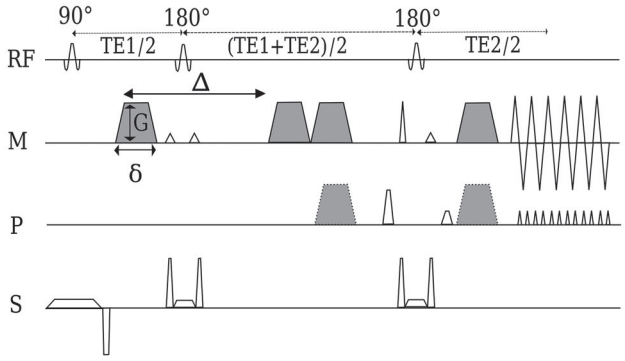

FIGURE 1 Schematic representation of the DDE sequence used in the study. The 4 gray filled-in diffusion encoding gradients have the same area although their orientation may vary: the orientation of the first pair defines the direction of the sequence while the relative angle ψ defines the angle between orientations of the first and second pairs. Imaging gradients (slice selection, echo planar imaging trajectory, and crushers) are displayed in white. In DDE-Asp the first pair (i.e., the direction) is maintained along the M axis and relative angles are such that the second pair lies in the MP plane which is perpendicular to asparaguses' stems. For each of the 3 orthogonal directions of DDE-Tum, the first pair is a linear combination of MPS directions. The second pair has the same orientation but with opposite or same polarity, corresponding to anti-parallel and parallel measurements, respectively

slew-rates of diffusion gradients were limited to 60 T/m/s while those of imaging gradients were limited to 100 T/m/s/.

All specimens were imaged using a 4-channel SENSE-compatible wrist coil for reception. The field of view was 130 × 130 mm with an in-plane resolution of 2 × 2 mm and 5 axial 4-mm thick slices. SENSE and echo planar imaging factors were 2 and 33, respectively. q-values are defined as $q = \gamma G\delta$ (in mm^{-1}), where γ is the gyromagnetic ratio of protons in MHz/T and G the gradient strength.

In asparaguses, 2 DDE protocols have been applied. The first is labeled DDE-Asp and was used to assess the accuracy of cell size estimation when using 5 relative angles in the plane perpendicular to asparaguses' stems. The second is labeled DDE-Asp P-AP and is the same as DDE-Asp but uses only 0 and 180° relative angles. Because these angles give rise to maximal signal difference for a specified cell size, the reduced dataset DDE-Asp P-AP is expected to yield satisfactory cell size estimations. The DDE-Asp has also been used in the 0°C phantom to assess its technical viability. A diffusion tensor imaging (DTI) scan was also performed.

In tumors, unpredictable global anisotropy may be present and measurements should be repeated in at least 3 orthogonal directions to smooth the anisotropy. To avoid tripling the scan time, our DDE protocol in tumors was limited to P-AP measurements. Furthermore, in tumors the effect of RD on signals is expected to be smaller than in asparaguses and estimations could, therefore, be more biased by gradient cross terms artifacts. Therefore, each measurement was performed a second time with all diffusion gradients having opposite polarity.[40] The total signal was taken as the geometric mean of signals from both polarities. Four signal averages were performed for each polarity (before the geometrical mean) leading to a total scan time of 11 min 38 s. This sequence is labeled DDE-Tum. A diffusion weighted imaging scan was also performed.

All the sequences details are given in Table 1.

Gradient intensities ranged from 0 to 80 mT/m in DDE-Asp and DDE-Tum. However, in DDE-Tum the 3 orthogonal directions were chosen to use a maximal strength of only 53.6 mT/m along each gradient axis to achieve a total strength of 80 mT/m (vector sum).

2.3 | Postprocessing

All images were denoised with Matlab® software using the algorithm described in Manjon et al[41] and freely available in Coupé.[42] After noise correction, tumor images were registered with a rigid transformation to correct for possible motion during MRI sessions.

2.4 | Tissue models

Models were written as dictionaries as in the Accelerated Microstructure Imaging via Convex Optimization (AMICO)

TABLE 1 Details of protocols used in the study[a]

Sequence	q-Values (mm^{-1})	b-Values ($ms/\mu m^2$)	δ/Δ (ms)	ψ (°)	Directions	TE/TR (ms)	Total # of meas.	NSA	Duration
DDE-Asp + 0 °C phantom	0, 7, 14, 21, 28, 35	0, 0.22, 0.87, 2.0, 3.5, 5.4	12/60	0, 45, 90, 135, 180	G1 along (0, 1, 0) G2 rotates in the {(0, 1, 0), (1, 0, 0)} plane	164/3000	26	8	11 m 23 s
DDE-Asp P-AP	0, 7, 14, 21, 28, 35	0, 0.22, 0.87, 2, 3.5, 5.4	12/60	0, 180	G1 and G2 along (0, 1, 0)	164/3000	11	8	4 m 49 s
DTI-Asp	–	0 and 0.8	11/29	–	32 isotropic	60/3000	33	2	6 m 59 s
DDE-Tum	0, 6.7, 13.3, 20, 26.7, 33.3, 40	0, 0.01, 0.39, 0.89, 1.58, 2.46, 3.55	13/32	0, 180	3 ⊥ (0.33, 0.67, −0.67) (−0.67, −0.33, −0.67) (−0.67, 0.67, 0.33)	108/2000	39 (13/dir)	8	11 m 38 s
DWI Tum	–	0 and 1	8/27	–	3 ⊥ (0.33, 0.67, −0.67) (−0.67, −0.33, −0.67) (−0.67, 0.67, 0.33)	55/2000	4	4	42 s

Abbreviation: DWI, diffusion weighted imaging.

[a]Directions are given in the fixed (x, y, z) frame of the scanner. G1 and G2 refer to the first and second diffusion encoding gradient pairs, respectively.

framework.[43,44] Signals were modeled using up to 3 compartments: an intracellular (ic), an extracellular (ec) and a vascular (va) compartment. The problem of estimating amplitudes ($\boldsymbol{x}$) of dictionary entries from experimental data $\boldsymbol{d}$ (column vector) can be written as:

$$\hat{\boldsymbol{x}} = \text{argmin}_{\boldsymbol{x}\geq 0} \|\mathbf{E}\boldsymbol{x} - \boldsymbol{d}\|_2^2 \quad (1)$$

with $\|\ldots\|_2$ being the Euclidean norm. The $\mathbf{E}$ matrix represents a dictionary and contains the attenuated diffusion signal for different measurements (rows) and different model parameters (columns), while components of the column vector $\boldsymbol{x}$ represent the amplitudes S_k of each dictionary entry. $\mathbf{E}$ is formed by the concatenation of 3 submatrices representing each compartment as:

$$\mathbf{E} = \left[\mathbf{E}^{ic} \left| \mathbf{E}^{ec} \right| \mathbf{E}^{va}\right] \quad (2)$$

All submatrices have N_d rows corresponding to the number of measurements in the experiment. Each compartment can also be evaluated for predefined values of a descriptor parameter P (e.g., cell radii), which fix the number of subdictionaries' columns to N_{ic}, N_{ec}, N_{va} for intracellular, extracellular and vascular compartments, respectively. Dimensions of the total dictionary are thus $N_d \times N_k$ ($N_k = N_{ic} + N_{ec} + N_{va}$) and its entries, attenuations $E(G(t), P)$ are computed for the corresponding gradient waveform $G(t)$ and descriptor parameter P before the estimation. Note that $G(t)$ represents the gradient waveform for a particular measurement. In this work, dictionaries have been calculated with an in-house Matlab implementation of the multiple correlation function method.[45,46] Finally, S_k's were estimated with the lsqnonneg Matlab function. No regularization has been used in the estimation (although it is often the case in AMICO experiments). Furthermore, positivity is the only constraint on the S_k's and signal fractions were obtained after normalization (see the Data analysis: MRI section).

- For asparaguses, intracellular sub-compartments were aligned cylinders of radii r_k with a diffusion coefficient fixed to 2 μm^2/ms, the value corresponding to free diffusion at 20°C. Twenty equidistant radii ($N_{ic} = 20$) in the interval [3;70] μm were used to ensure full coverage of the size distribution. Extracellular sub-compartments were hindered diffusion environments with 5 equidistant diffusivities D_k ($N_{ec} = 5$) in the interval [1;2] μm^2/ms. There was no vascular compartment. This leads to $N_k = 25$ different S_k's to estimate with 26 measurements (c.f., Table 1). Note that with DDE-Asp P-AP, 25 S_k's are to be estimated with only 11 measurements. In this case, the underdetermined system is solved by taking the minimum norm solution in the algorithm of the lsqnonneg function.
- For tumors, intracellular sub-compartments were modeled as impermeable spheres with 5 radii r_k equidistant in [5;20] μm with a diffusion coefficient fixed to 2 μm^2/ms and extracellular sub-compartments represented hindered diffusion environments with 4 diffusivities D_k equidistant in [1;2] μm^2/ms. For the vascular compartment, we used the following expression:

$$E^{va}\left(G;\, v_k\right) = E_{Sticks}\left(G;\, D_B\right) . \left|\text{sinc}\left(\gamma \alpha\left(G\right) v_k/\pi\right)\right| \quad (3)$$

with 4 v_k evenly spaced velocities from 2 to 5.10^{-4} m/s. In Equation 3, E_{Sticks} is the signal attenuation due to diffusion in blood vessels and was calculated for randomly orientated sticks. The blood diffusion coefficient D_B was set to 1.75 μm^2/ms.[30] The sinc modulation is valid for randomly orientated vessels displaying plug flow velocity v_k[47] in the ballistic regime. The factor $\alpha(G)$ is defined by:

$$\alpha\left(G\right) = \int_0^{TE} G\left(t\right) t dt \quad (4)$$

This leads to $N_k = 13$ different S_k's to estimate with 13 measurements per direction (c.f., Table 1).

To shed some light on accuracy and precision of the fitting procedure itself, simulations have been performed to check the robustness of the fitting procedure. These are presented separately in the Supporting Information Figure S1 section available in the online version of the article.

Consider a DDE experiment with fixed Δ and minimal t_m. When RD is present, a positive signal difference S(ψ = 180°)-S(ψ = 0°) occurs.[18,20] As explained in Ahlgren et al,[30] the ψ = 0° measurement is flow compensated and has $\alpha = 0$ while its equivalent with ψ = 180° is not flow compensated and has $\alpha > 0$. In this case, further attenuation is caused by any ballistic flow and a negative difference between 180° and 0° signals could appear. However, in the pseudo-diffusion regime, perfusion appears like Gaussian diffusion and no signal difference between 180° and 0° can be observed. Clearly, the diffusion time Δ determines the regime: ballistic (short Δ) or pseudo-diffusion (long Δ). Most diffusion MRI applications use intermediate Δ, where best practice would be to use 1 compartment for each of these 2 regimes. In this work, we tested the sensitivity to ballistic flow and always use 1 ballistic compartment (see Equations 2 and 3), although it may only reflect a fraction of the actual perfusion.

2.5 | Data analysis: MRI

Diffusion coefficients in the 0°C phantom were estimated on the basis of second order polynomial fittings of the MR signal's logarithm versus q-value[48] and compared with the reference value at 0°C, 1.099 μm^2/ms.

To locate aligned cylindrical structures in asparaguses, voxels of the PE were automatically segmented using 2

criterions based on a heuristic: a minimal signal intensity of 30% of the maximal image intensity to allow sufficient signal-to-noise ratios (SNRs) and a minimal fractional anisotropy of 0.2 with the main eigenvector oriented in the z-direction. Fractional anisotropy and eigenvectors were computed from the DTI sequence data.[48] The following parameters were calculated from DDE-Asp:

$$f_{ic}=\frac{\sum_{k=1}^{N_{ic}} S_{ic,k}}{\sum_{k=1}^{N_{ic}} S_{ic,k}+\sum_{k=1}^{N_{ec}} S_{ec,k}};\quad f_{ec}=\frac{\sum_{k=1}^{N_{ec}} S_{ec,k}}{\sum_{k=1}^{N_{ic}} S_{ic,k}+\sum_{k=1}^{N_{ec}} S_{ec,k}};$$
$$D_{ec}=\frac{\sum_{k=1}^{N_{ec}} S_{ec,k}D_k}{\sum_{k=1}^{N_{ec}} S_{ec,k}};\quad PSD_k=\frac{S_{ic,k}}{r_k^2};\quad R=\frac{\sum_{k=1}^{N_{ic}} PSD_k.r_k}{\sum_{k=1}^{N_{ic}} PSD_k} \tag{5}$$

where f_{ic}, f_{ec}, D_{ec}, PSD_k, and R are the total intracellular and extracellular fractions, the diffusivity in the extracellular matrix, the pore size distribution (PSD), and the mean radius, respectively. Note that in the calculation of PSD_k, the volume weighting of cylinders or spheres has been taken into account by dividing by r_k^2 or r_k^3 in asparaguses or tumors, respectively.[49] Asparagus analysis was repeated but using only P-AP measurements from DDE-Asp to investigate the influence of reducing the dataset on estimated parameters.

Before applying any model analysis, the sensitivity of DDE-Tum to RD and ballistic flow was assessed. In a medium, like asparaguses, where only RD is present, signal differences, *S(180°)-S(0)* are expected to be strictly positive. In contrast, if ballistic flow is present, decreased or even negative differences could be observed. Thus, we evaluated those differences for highest and lowest q-values. To exclude the possibility that differences are due to sequence artifacts, those were also measured in the wrist coil phantom where they should be zero.

Model parameters of Equation 5 were calculated from DDE-Tum but taking also the vascular compartment into account for normalization of f_{ic} and f_{ec}. In addition, the total vascular fraction f_{va} and the mean flow velocity v were evaluated by:

$$f_{va}=\frac{\sum_{k=1}^{N_{va}} S_{va,k}}{\sum_{k=1}^{N_{ic}} S_{ic,k}+\sum_{k=1}^{N_{ec}} S_{ec,k}+\sum_{k=1}^{N_{va}} S_{va,k}};\quad v=\frac{\sum_{k=1}^{N_{va}} S_{va,k}v_k}{\sum_{k=1}^{N_{va}} S_{va,k}} \tag{6}$$

Parametric maps were constructed for each direction of DDE-Tum (see 'MRI' section) and then averaged over the 3 orthogonal directions. Regions of interest (ROIs) of low perfusion were manually traced on the f_{va} maps in which corresponding R and f_{ic} values were also evaluated.

2.6 | Histology

After MRI (resp. extraction), asparaguses (resp. tumors) were immediately immersed in a 10% formaline buffer solution for fixation. Three-millimeter resections were taken at the location that was aligned with the central MRI slice. Those samples were then embedded in paraffin and 4-µm-thick slices were cut with a Leica rotary microtome. A hematoxylin-eosin (HE) staining was finally performed for comparison with MRI central slices. Whole slide photomicrographs in 40× magnification were obtained using an automatic scanner (Leica SCN400). Analyses of histology micrographs were done with ImageJ.[50]

For quantifying cell sizes in asparaguses, a total of 1048 cells were automatically segmented by thresholding the image intensity. Next, the particle analyzer plug-in was used to calculate segmented areas which were converted to radii of equivalent section disks. The PSD was then calculated as the normalized histogram of radii.

In tumors, ischemic necrosis areas resulting from vascular depletion were identified on HE micrographs by the presence of damaged blood vessels surrounded by pyknotic cells. Therein, vessels are dilated with irregular and depleted membranes and contain practically no functioning red blood cells that are intensely stained in red by the eosin in normal conditions. Furthermore, nuclei show dense hematoxylin staining due to chromatin condensation (pyknosis), which indicates their decay.

For each tumor, cell sizes and intracellular fractions were evaluated in viable and necrotic regions by taking rectangular fields of 600×330 µm^2 in each region. In each field, 25 cells displaying clear boundaries were manually segmented and minimal Feret diameters were calculated with the Measure tool of ImageJ. In 2 dimensions, the Feret diameter is the distance between 2 infinite parallel lines pinching an object (like a caliper). The minimal Feret diameter is the minimal distance measured over all possible orientations of the parallel lines. As tumor cells may present fusiform shapes, this metric is more relevant than the averaged radius as it is less sensitive to cell orientation in the image plane.[51] To evaluate the intracellular fraction, each field was divided in 8 identical rectangles in which the fraction of stained area was calculated. Correlation data were obtained from manually placed voxels on f_{va}-maps corresponding approximately to positions of the fields on the HE maps. Note that automatic placement of voxels could not be done as DDE maps and histology micrographs are distorted by echo planar imaging susceptibility artifacts and tissue processing, respectively.

2.7 | Statistics

Parameters' distributions of the study are shown using their histogram or boxplots. In the latter case, a blue box indicating Q_1 (25th) and Q_3 (75th) quartiles surrounds the median while whiskers indicate all measurements excluding outliers. Those are defined as points higher than Q_3+1.5*IQR or lower than

$Q_1-1.5*IQR$, where IQR is the inter-quartile range. Medians of distributions were compared with a left or right-sided Wilcoxon rank sum test to assess the significant superiority or inferiority of 1 median over another. Tests for zero medians were done with a Wilcoxon signed rank test. In tables and figures, symbols * or ** were used to indicate a *P*-value smaller than 0.05 or 0.01. Pearson's linear correlation coefficients were calculated with the corr Matlab function.

3 | RESULTS

ADC measurements from DDE-Asp in the 0°C phantom yielded a median error of 3.9% (q_1 = 3.5%; q_3 = 4.2%). Measurements on asparaguses are shown in Figure 2. Only voxels from the PE mask (Figure 2C) were analyzed. The model fitting yielded a signal (i.e., calculated from Equation 1) that closely matched the measured signal (Figure 2D). From Figure 2D, it can be noted that signal differences between parallel and anti-parallel measurements grow with q and are positive. PSD's estimated from full (6 q-values and 5 ψ) and P-AP measurements are depicted in Figure 2E and their corresponding quartiles and mean sizes are shown in Table 2. Differences in quartiles or mean sizes never exceeded 2% between the full and P-AP analyses and, in both cases, were typically less than 6% when compared with LM. Pearson's linear correlation coefficients between parameters from each voxel between the 2 analyses are displayed in Table 3. High correlations were observed between microstructural parameters. The coefficient is, however, slightly smaller for *R*.

Signal differences between parallel and anti-parallel measurements were evaluated for DDE-Tum in tumors and a wrist coil water phantom. Resulting histograms and their

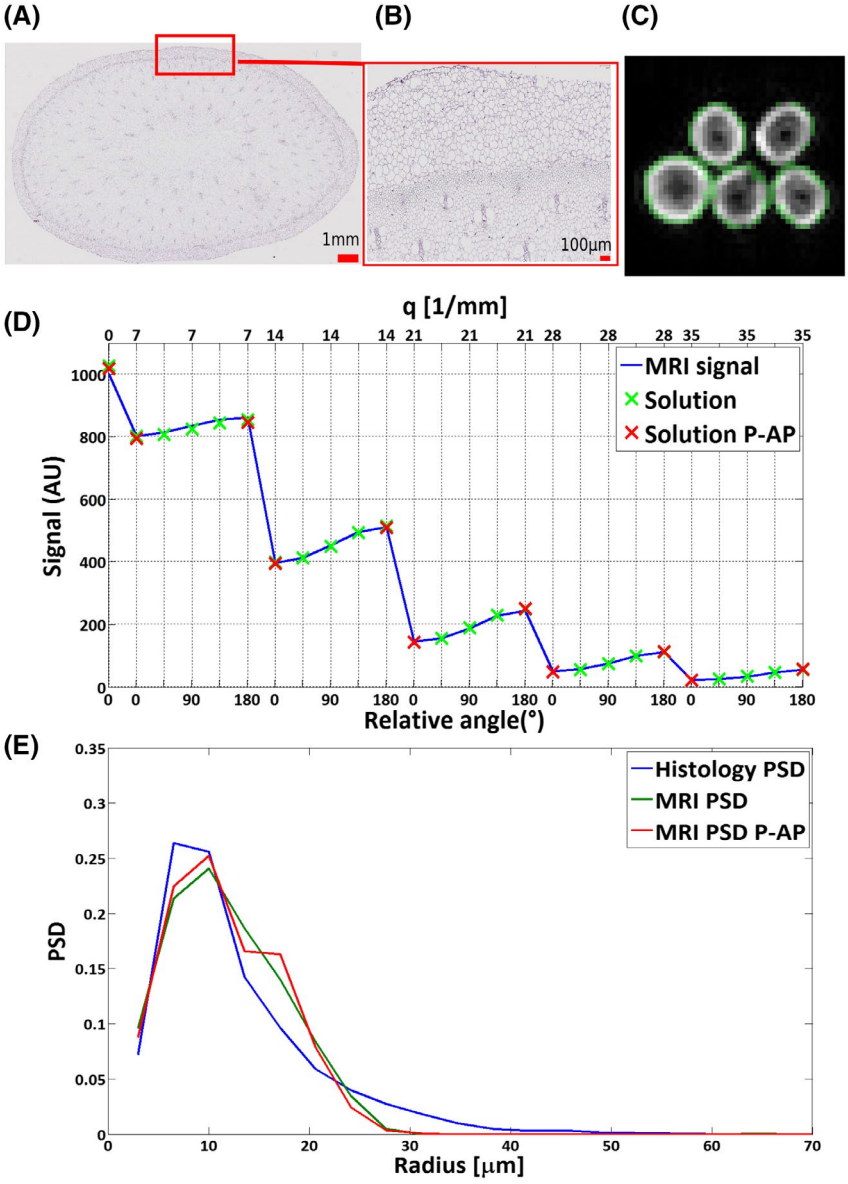

FIGURE 2 HE stain micrographs of an asparagus's stem (A) and a zoom on the PE (B). C, T2-weighted (q = 0) MR image of asparaguses along with the mask of the PE in green. D, Curves of the measured signal averaged over the PE, the solution yielded by the model analysis using 6 q-values and 5 ψ and the solution yielded by the same model analysis but using only P-AP measurements. Note the 2 x-axes representing varying q-values and relative angles ψ. E, PSDs (averaged over the PE) derived from histology, DDE-Asp analysis, and DDE-Asp analysis using only parallel and anti-parallel relative angles

medians are presented in Figure 3. Lowest (6.67 mm^{-1}) and highest (40 mm^{-1}) q-values were selected as the effect of RD (i.e., positive difference) is supposed minimal and maximal in those respective conditions. Differences were obtained throughout either tumors or the phantom and each of the 3 orthogonal directions. For the lowest (highest) q-value, medians in tumors were always negative (positive) and inferior (superior) to medians in the phantom.

The model analysis from DDE-Tum measurements is presented in Figure 4. Necrotic regions are indicated by arrows in Figure 4A and appeared globally consistent with ROIs of low vascular fraction from DDE-Tum (Figure 4B. Intracellular fraction and mean cell radii were also both significantly ($P < 0.01$) decreased in necrotic ROIs compared with these of viable tissue. This decrease was confirmed when evaluating fractions of stained areas and minimal Feret diameters in HE micrographs (Figure 5A,B). Illustrations of necrosis, fraction of stained area calculations and the manual cell segmentation are shown in Figure 5C-E. Correlation between voxels and fields from histology is presented in Figure 6. It can be seen that there is a high correlation for the intracellular fraction f_{ic}, but a lower correlation can be observed for the cell size (but still significant). Maps of the 6 parameters estimated with DDE-Tum are shown in Figure 7. A common pattern is clearly seen between f_{ic}, f_{va}, f_{ec}, and D_{ec} which is globally consistent with necrotic and viable areas delimited in Figure 4A. Although a significant decrease of R was observed in the necrotic ROI, values look more heterogeneous therein. In turn, v clearly dropped in the necrotic ROI of the right tumor but not in the left one. Those latter observations are consistent with the higher sensitivity of R and v to noise and the poor differentiation of v between viable and necrotic tissues highlighted in the simulations (c.f., Supporting Information Figure S1).

TABLE 2 Quartiles of PSD's averaged over the PE from analyses using LM or full or P-AP MRI measurements

PSD quartiles and mean radii (μm)	Q_1	Q_2 (median)	Q_3	R
LM	7.50	10.85	16.28	12.61
PSD from full measurements	7.83	11.52	16.01	11.73
PSD from P-AP measurements	7.76	11.32	16.01	11.62

TABLE 3 Pearson's linear correlation coefficients between parameters from analyses using full or P-AP measurements

Model parameter	f_{ic}	f_{ec}	R	D_{ec}
Pearson's correlation coefficient	0.9879**	0.9847**	0.8581**	0.9781**

4 | DISCUSSION AND CONCLUSIONS

Multi-compartment analyses offer a unique possibility to characterize tissue microstructure. However, they are usually ill-conditioned or ill-posed which affects their specificity. Despite being highly sensitive, diffusion MRI's outcomes must be carefully interpreted in terms of the actual tissue morphology. Tumor microenvironment is generally too complicated to be accurately modeled in multi-compartment

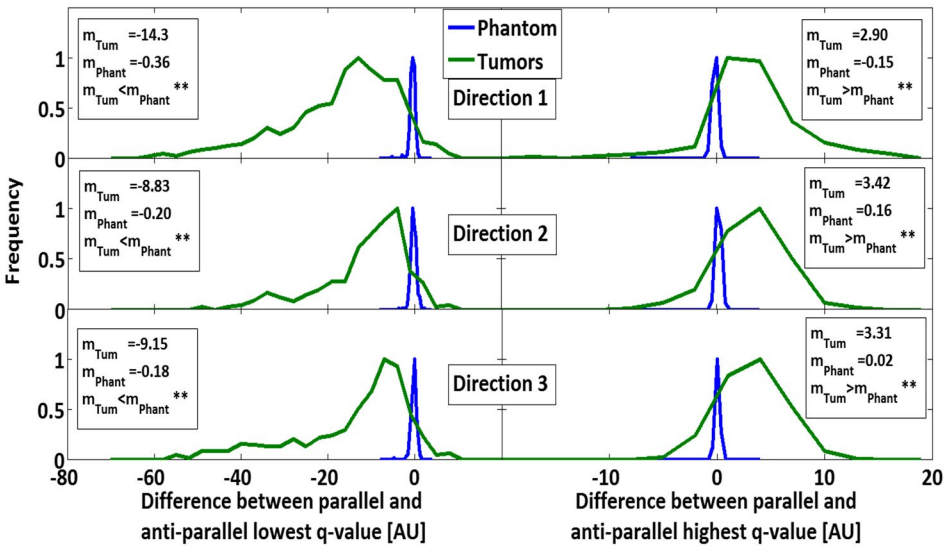

FIGURE 3 Changes between MR signals for 0 and 180° relative angles for lowest (6.67 mm^{-1}) (left) and highest (40 mm^{-1}) (right) q-values, i.e., *S(180°)-S(0)*. Values are averaged over the whole phantom or the 2 tumors. The 3 plots correspond to the 3 gradient directions

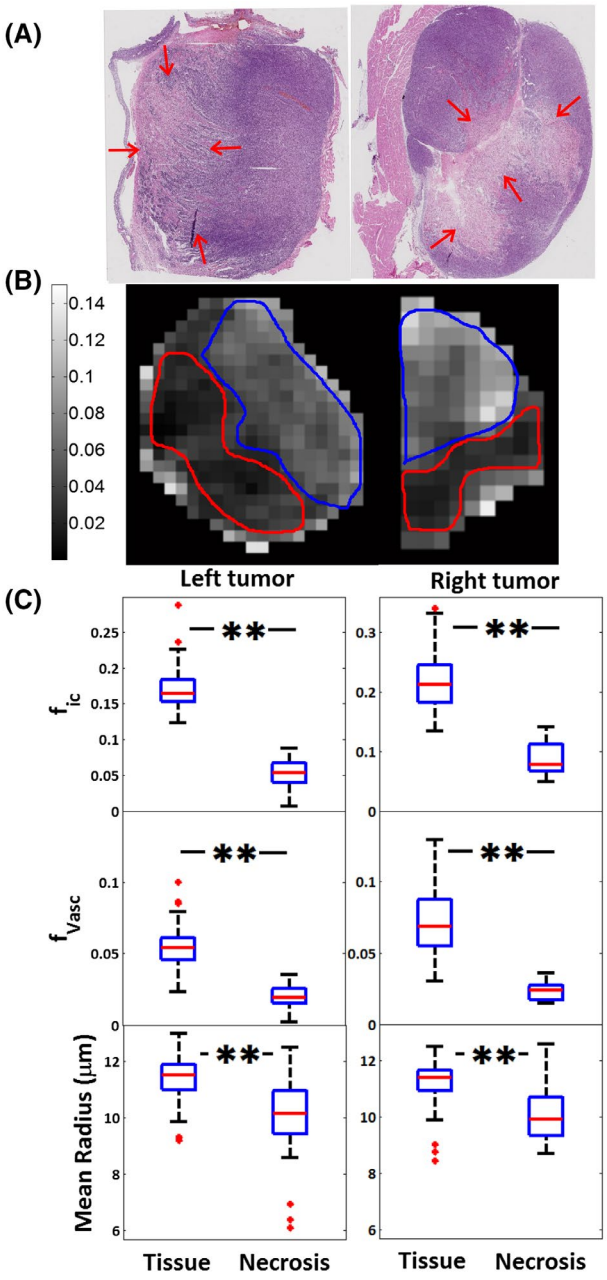

FIGURE 4 A, HE stain micrographs of whole tumors corresponding to the central MRI slice. Arrows indicate areas of ischemic necrosis. B, Maps of the f_{va} parameter along with ROIs delineating parts of high (blue) and low (red) vascular fractions. C, Boxplots of f_{ic}, f_{va} and R parameters estimated from the diffusion model in each ROI

analyses. Indeed, the following features were not taken into account in our model but may have an impact on diffusion measurements: cell nuclei,[52] actual cell shape,[53] cell membrane permeability,[54,55] and anisotropy due to collagen in the extracellular matrix [56] or due to the vascular environment.[57] Embedding all these features in 1 model is challenging, especially for clinical applications where scan time, and thus SNR, is limited. In this context, testing our DDE sequence on asparaguses was relevant to assess its ability to quantify cell sizes. Of course, this does not give any insight on DDE's performance in vivo but is necessary for DDE to be relevant in tumors. Together with ADC measurements in the 0°C phantom, this analysis served as a calibration step in the implementation of our DDE sequence in tumors. Furthermore, it indicated that parallel and anti-parallel measurements were sufficient to robustly estimate, at least, the cell sizes.

The model used in tumors of this study is isotropic. However, global anisotropy may be present in tumors although its origin is not obvious or explained by a single factor.[58] For instance, collagen, vascular network or aligned elongated cells have been shown as possible causes of anisotropy.[59] Modeling global anisotropy also requires more parameters to be estimated. We simplified the problem by using an isotropic model and taking only P-AP measurements in 3 orthogonal directions to calculate directional averages of estimated parameters. Another possibility would be to average signals over the directions first and then estimate the resulting parameters. However, we did not prefer this option because the multi-compartment model contains parameters of different types (scalars, second-order tensors, …) needing at least theoretically different types of directional averaging.

The diffusion time influences the regime under which RD and vasculature appear on measurements. To hypothesize ballistic flow, Δ must be sufficiently short. Conversely, working with a pseudo-diffusion model suggests that Δ is sufficiently long. We tested the sensitivity to ballistic flow of our DDE-Tum protocol independently of any diffusion model by simply examining differences between signals from P-AP measurements. For high q-values, the effect of RD is dominant and positive signal differences are observed in tumors as well as asparaguses. However, for low q-values negative differences appear which cannot be explained by a sequence artifact, as indicated by the results in the wrist coil phantom. We, therefore, attribute the observed negative signal differences to the presence of ballistic flow. Of course, this does not exclude a partial influence of pseudo-diffusion on the signal: any diffusion sequence that uses intermediate Δ may be contaminated by both regimes of micro-vascular flow. Adversely, using long Δ may lead to severe SNR drop due to T_2 relaxation and possible influence of membrane permeability on size estimates. A possible way to deal with intermediate Δ would be to use and extended model of the vascular compartment where both regimes are taken into account at the price of a more complicated parameter estimation procedure.

The final step of the study was to investigate whether morphological differences present within tumors were reflected in the model parameters estimated from the DDE-Tum protocol. On HE stained micrographs, blood supply depleted areas were associated with a decrease of both intracellular fraction and mean cell size. This was also observed in ROIs segmented on

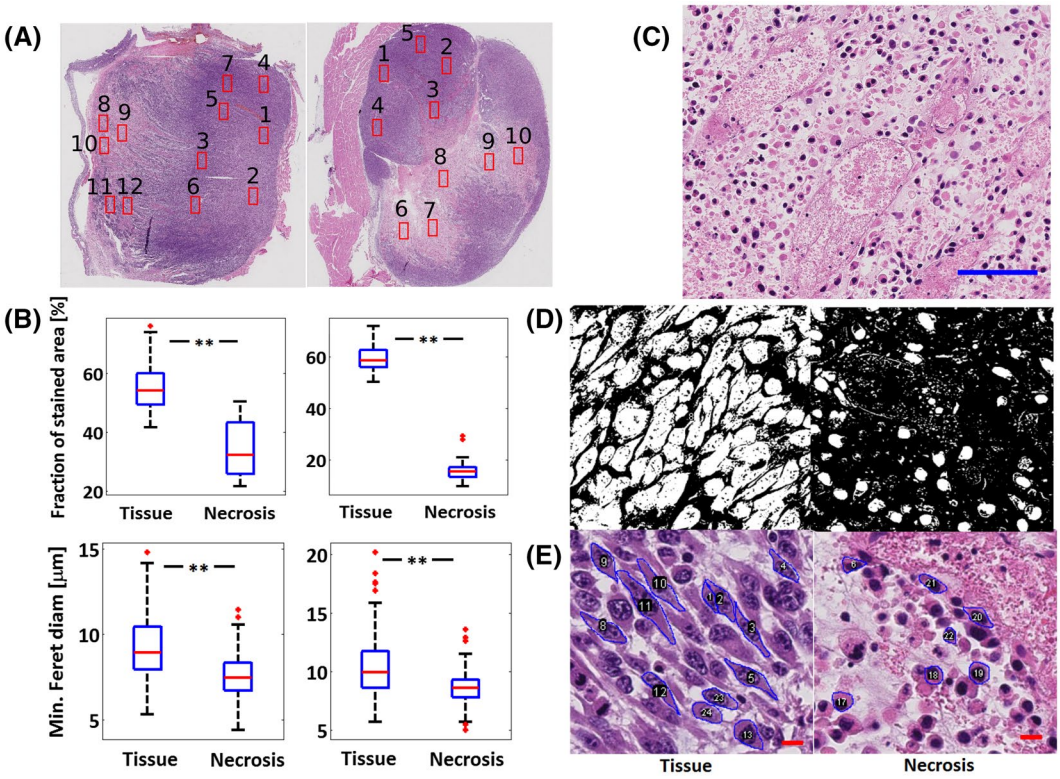

FIGURE 5 A, HE stain micrographs of whole tumors along with the fields used for histology analyses at 40× magnification. Fields were used in viable tissue and in necrosis. B, Boxplots of staining fractions and minimal Feret diameters in the fields corresponding to viable tumor tissue or necrosis. C, Illustration micrograph of a necrosis area displaying pyknotic nuclei and necrotic tumor cells and blood vessels. The blue bar is 100 microns. D, Illustrations of binary micrographs obtained from thresholding image intensities. Intracellular fractions are defined as the percentage of white pixel. E, Illustration of manually segmented cells. Note the fusiform shape that may be encountered in some cells. The red bar is 10 microns. The minimal Feret diameter was calculated with the Measure function of ImageJ. Note that Figure 5D,E are not taken in the same field

vascular fraction maps and consistent with areas of ischemic necrosis on HE micrographs. The drop of the intracellular fraction is generally expected in necrotic regions. The evolution of dying cell morphology under hypoxia is subtler as several cell death pathways may be possible.[60] Evaluating the precise physiology governing decaying tissues in our tumors was out of the scope in this study. Thus, no expectations could be made regarding variation in cell sizes. Instead, we simply evaluated cell size changes between infarcted and viable tumor tissues at a particular time and found that histology was consistent with DDE results.

The correlation plots showed a good correlation for intracellular fraction but a somewhat lower correlation for cell size. Part of the explanation for this decreased correlation might be the fact that minimum Feret diameter and cell radius R of a spherical cell in our model are not completely equivalent quantities.

Time-dependent diffusion is currently a popular technique where gradient waveforms are designed to probe diffusion at different diffusion times.[16] The relationship between the mean squared spins' displacement and the diffusion time is linear for free diffusion but becomes highly dependent on restriction sizes for spins encountering cell membranes. This sensibility to pore size is exploited in models like VERDICT, IMPULSED, or both (see POMACE in Reynaud et al[61]). The proposed DDE sequence does not exploit time-dependent diffusion but rather relies on the influence of RD on P-AP measurements at a constant Δ. For low to moderate b-values as used in our work (tumors), it is not obvious that DDE would carry more information than multiple Δ single diffusion encoding.[62] However, it could be safer to work with constant Δ in practice. Indeed, modeling tissue using a sequence with varying Δ requires some cautions as the extracellular compartment cannot, in theory, be accurately modeled with a constant diffusivity.[16] Furthermore, we mentioned earlier that the vascular compartment may be modeled either by ballistic flow or pseudo-diffusion, depending on Δ. The use of a single Δ instead of varying Δ could be an advantage as both regimes will give constant contributions to the MR signals. Therefore, the proposed DDE sequence is not expected to convey more information than time-dependent diffusion but it could offer a more accurate way to model extracellular and vascular compartments.

Absolute quantification of microstructural parameters from diffusion measurements is difficult because model

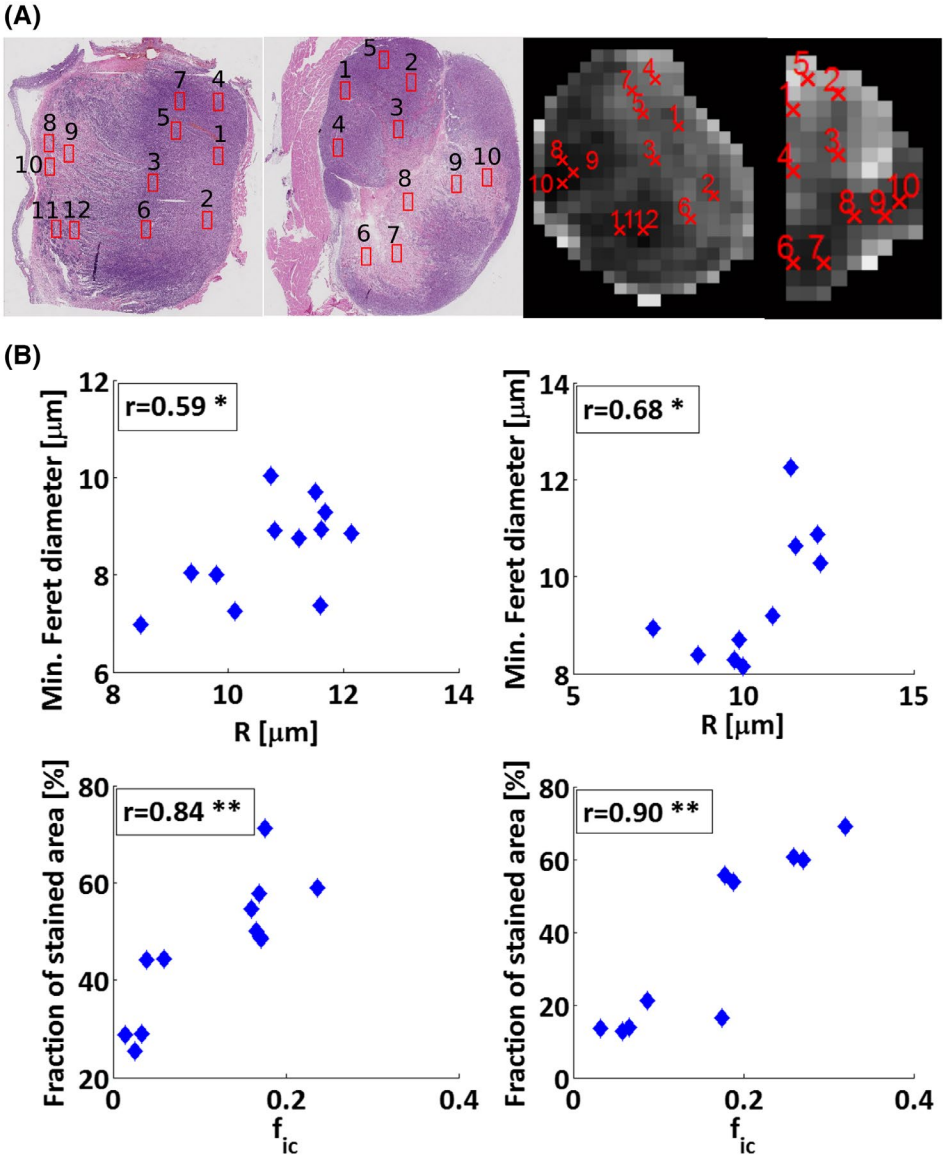

FIGURE 6 A, Left panels show positions of the fields used to calculate minimal Feret diameters and percentage of stained area. Right panels display pixels that were placed manually on the map of f_{va} to approximatively correspond to fields of HE maps. B, Correlation data between DDE and mean histology estimates of each field. In the graphs, r represents the Pearson correlation coefficient

parameters may inherently depend on the MR pulse sequence parameters. For instance, compartment fractions are weighted by T_2 relaxation, which may not be the same in each compartment. Similarly, size estimates may be biased by membrane permeability as Δ is increased. Finally, the influence of Δ on the vascular compartment was discussed earlier. Our main interest in diffusion modeling is rather to investigate whether variations in estimated parameters are accurate biomarkers of actual microstructural evolutions. Although model parameters estimated from our DDE sequence indicated to yield consistent sensitivity to RD and ballistic flow perfusion within tumors presenting ischemic necrosis, their clinical relevance in assessing physio-pathological evolutions (for instance, during therapy) has to be tested. In future works, this DDE protocol should be evaluated at several time points on large cohorts of tumors separated at least in treated and control groups.

Our study mainly investigated the technical feasibility of a DDE sequence sensitive to RD and ballistic flow for estimating tumors' microstructural parameters on a clinical scanner. However, clinical relevance can only be assessed in human studies. In clinical practice, a lot of problems can arise depending on the circumstances, e.g., motion, body fat, etc. To avoid the associated artifacts, modification of the sequence will be necessary. Furthermore, T_2 is typically around 100 ms in tumors which corresponds to the TE used in tumors of this study (108 ms) but means that our DDE protocol may suffer from strong signal attenuation in some applications. In such cases regularization, which was not used here, should be used to stabilize the estimations. Although 5 slices were enough

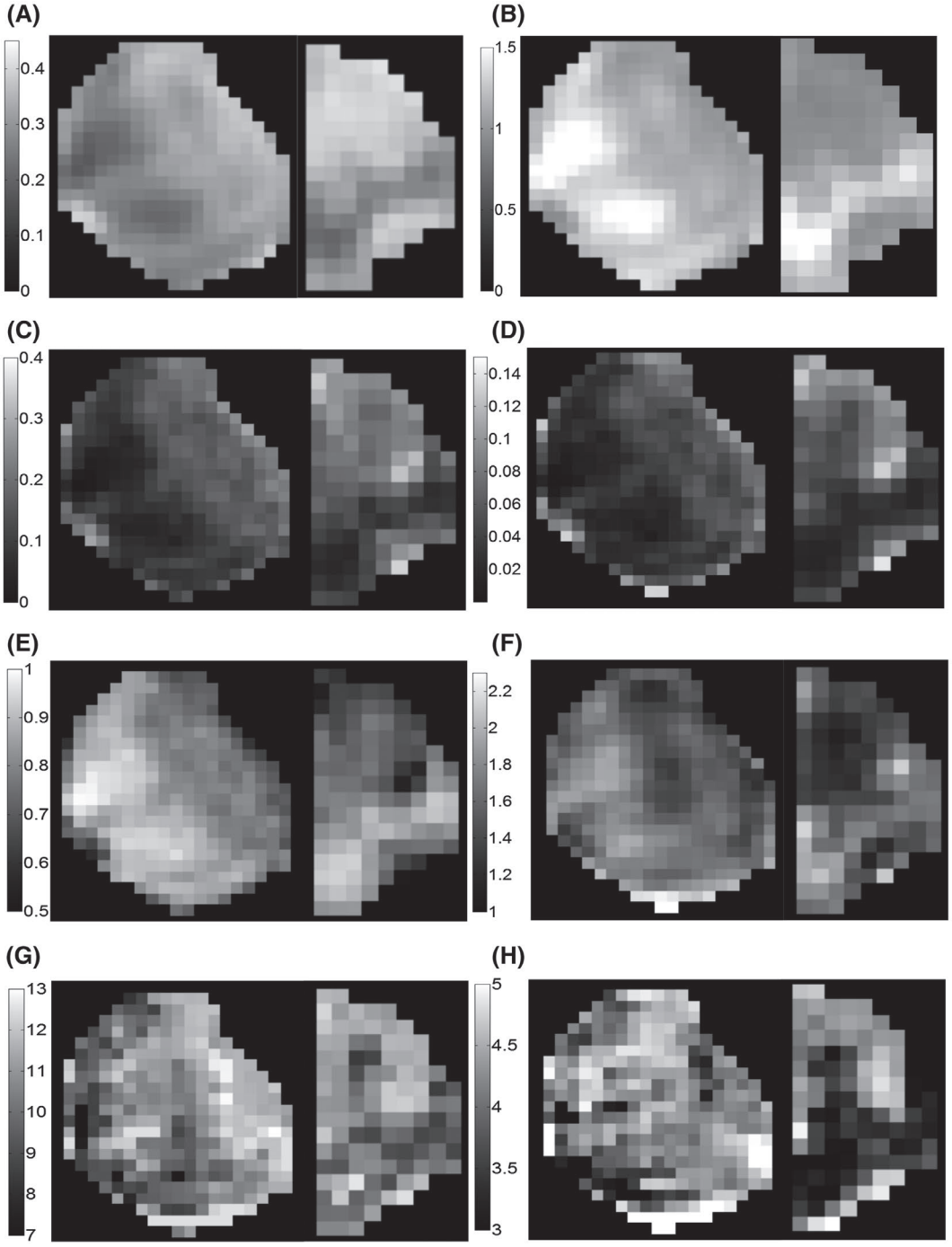

FIGURE 7 Parametric maps derived from the diffusion model for right and left tumors. Diffusion weighted maps (A), ADC from b = 0 and 1 ms/μm^2 (in μm^2/ms) (B), f_{ic} (C), f_{va} (D), f_{ec} (E), D_{ec} in μm^2/ms (F), R in μm (G), and v in ×100 μm/s (H)

for tumors' coverage, up to 10 slices could be used within the TR of DDE-Tum (2000 ms). Using more slices would increases the scan time. As a result, our DDE-Tum sequence should be considered as a first step to clinical application.

In conclusion, we presented a pilot study of a DDE protocol implemented on a clinical scanner for noninvasive characterization of tumors' microenvironment based on an adapted AMICO-VERDICT analysis. The DDE protocol exploited the limited gradient strength available on clinical scanners and was constrained to have a scan time acceptable for clinical practice (and thus having suboptimal SNR). The technical viability of the sequence was first investigated as well as its ability to robustly quantify cell sizes in simple tissue morphologies (asparaguses). Results of this quantification were confirmed by LM and were only weakly affected by reducing the dataset to P-AP measurements which allows DDE to be performed in several directions to cope with global anisotropy within an acceptable scan time. After

this primary validation, analysis of DDE's signal attenuation demonstrated the sensitivity of DDE to RD and ballistic flow. The microstructure model parameters were estimated in 2 allografts of rhabdomyosarcoma. DDE's outcomes clearly showed differentiation between viable and decaying tissue following ischemic necrosis that was confirmed by histology. These encouraging results will serve as a basis to investigate subtler physio-pathological mechanisms occurring during radiotherapy in a future study.

ORCID

Gaëtan Duchêne https://orcid.org/0000-0001-9285-8319

REFERENCES

1. Le Bihan D, Turner R, Douek P, Patronas N. Diffusion MR imaging: clinical applications. *AJR Am J Roentgenol*. 1992;159:591–599.
2. White NS, McDonald CR, Farid N, et al. Diffusion-weighted imaging in cancer: physical foundations and applications of restriction spectrum imaging. *Cancer Res*. 2014;74:4638–4652.
3. Le Bihan D. Magnetic resonance diffusion imaging: introduction and concepts. In: Jones D, ed. *Diffusion MRI: Theory, Methods and Applications*. New York: Oxford University Press; 2011:57–78.
4. Surov A, Meyer HJ, Wienke A. Correlation between apparent diffusion coefficient (ADC) and cellularity is different in several tumors: a meta-analysis. *Oncotarget*. 2017;8:59492–59499.
5. Niendorf T, Dijkhuizen R, Norris D, Van Lookeren CM, Nicolay K. Biexponential diffusion attenuation in various states of brain tissue: implications for diffusion weighted imaging. *Magn Reson Med*. 1996;36:847–857.
6. Le Bihan D. The 'wet mind': water and functional neuroimaging. *Phys Med Biol*. 2007;52:R57.
7. Kiselev VG, Il'yasov KA. Is the "biexponential diffusion" biexponential? *Magn Reson Med*. 2007;57:464–469.
8. Assaf Y, Basser PJ. Composite hindered and restricted model of diffusion (CHARMED) MR imaging of the human brain. *NeuroImage*. 2005;27:48–58.
9. Zhang H, Schneider T, Wheeler-Kingshott CA, Alexander DC. NODDI: practical in vivo neurite orientation dispersion and density imaging of the human brain. *NeuroImage*. 2012;61:1000–1016.
10. Assaf Y, Blumenfeld-Katzir T, Yovel Y, Basser PJ. Axcaliber: a method for measuring axon diameter distribution from diffusion MRI. *Magn Reson Med*. 2008;59:1347–1354.
11. Alexander DC, Hubbard PL, Hall MG, et al. Orientationally invariant indices of axon diameter and density from diffusion MRI. *NeuroImage*. 2010;52:1374–1389.
12. Le Bihan D, Breton E, Lallemand D, Grenier P, Cabanis E, Laval-Jeantet M. MR imaging of intravoxel incoherent motions: application to diffusion and perfusion in neurologic disorders. *Radiology*. 1986;161:401–407.
13. Le Bihan D. What can we see with IVIM MRI? *NeuroImage*. 2019;187:56–67.
14. Panagiotaki E, Walker-Samuel S, Siow B, et al. Noninvasive quantification of solid tumor microstructure using VERDICT MRI. *Cancer Res*. 2014;74:1902–1912.
15. Panagiotaki E, Chan RW, Dikaios N, et al. Microstructural characterization of normal and malignant human prostate tissue with vascular, extracellular, and restricted diffusion for cytometry in tumours magnetic resonance imaging. *Invest Radiol*. 2015;50:218–227.
16. Reynaud O. Time-dependent diffusion MRI in cancer: tissue modeling and applications. *Front Phys*. 2017;5. https://doi.org/10.3389/fphy.2017.00058.
17. Jiang X, Li H, Xie J, et al. In vivo imaging of cancer cell size and cellularity using temporal diffusion spectroscopy. *Magn Reson Med*. 2017;78:156–164.
18. Callaghan P. *Translational Dynamics and Magnetic Resonance: Principles of Pulsed Gradient Spin Echo NMR*. New York: Oxford University Press; 2011.
19. Koch MA, Finsterbusch J. Compartment size estimation with double wave vector diffusion-weighted imaging. *Magn Reson Med*. 2008;60:90–101.
20. Koch MA, Finsterbusch J. Towards compartment size estimation in vivo based on double wave vector diffusion weighting. *NMR Biomed*. 2011;24:1422–1432.
21. Benjamini D, Katz Y, Nevo U. A proposed 2D framework for estimation of pore size distribution by double pulsed field gradient NMR. *J Chem Phys*. 2012;137:224201.
22. Shemesh N, Ozarslan E, Basser PJ, Cohen Y. Accurate noninvasive measurement of cell size and compartment shape anisotropy in yeast cells using double-pulsed field gradient MR. *NMR Biomed*. 2012;25:236–246.
23. Komlosh ME, Özarslan E, Lizak MJ, et al. Mapping average axon diameters in porcine spinal cord white matter and rat corpus callosum using d-PFG MRI. *NeuroImage*. 2013;78:210–216.
24. Weber T, Ziener CH, Kampf T, Herold V, Bauer WR, Jakob PM. Measurement of apparent cell radii using a multiple wave vector diffusion experiment. *Magn Reson Med*. 2009;61:1001–1006.
25. Methot V, Ulloa P, Koch MA. Pore size estimation from double diffusion encoding. *Curr Dir Biomed Eng*. 2017;3:627–630.
26. Ianuş A, Drobnjak I, Alexander DC. Model-based estimation of microscopic anisotropy using diffusion MRI: a simulation study. *NMR Biomed*. 2016;29:672–685.
27. Ianus A, Shemesh N, Alexander DC, Drobnjak I. Double oscillating diffusion encoding and sensitivity to microscopic anisotropy. *Magn Reson Med*. 2017;78:550–564.
28. Coelho S, Pozo JM, Jespersen SN, Jones DK, Frangi AF. Resolving degeneracy in diffusion MRI biophysical model parameter estimation using double diffusion encoding. *Magn Reson Med*. 2019;82:395–410.
29. Shemesh N, Jespersen SN, Alexander DC, et al. Conventions and nomenclature for double diffusion encoding NMR and MRI. *Magn Reson Med*. 2016;75:82–87.
30. Ahlgren A, Knutsson L, Wirestam R, et al. Quantification of microcirculatory parameters by joint analysis of flow-compensated and non-flow-compensated intravoxel incoherent motion (IVIM) data. *NMR Biomed*. 2016;29:640–649.
31. Yang G, Tian Q, Leuze C, Wintermark M, McNab JA. Double diffusion encoding MRI for the clinic. *Magn Reson Med*. 2018;80:507–520.
32. Chenevert TL, Galbán CJ, Ivancevic MK, et al. Diffusion coefficient measurement using a temperature-controlled fluid for quality control in multicenter studies. *J Magn Reson Imaging*. 2011;34:983–987.

33. Holz M, Heil SR, Sacco A. Temperature-dependent self-diffusion coefficients of water and six selected molecular liquids for calibration in accurate 1H NMR PFG measurements. *Phys Chem Chem Phys*. 2000;2:4740–4742.
34. Levetin E, McMahon K. The plant body. In: Levetin E, McMahon K, eds. *Plants and Society*. Boston: McGraw-Hill Higher Education; 2008.
35. Panagiotaki E, Hall MG, Zhang H, Siow B, Lythgoe MF, Alexander DC. High-fidelity meshes from tissue samples for diffusion MRI simulations. *Med Image Comput Comput Assist Interv*. 2010;13(Pt 2):404–411.
36. Blasberg CH. Phases of the anatomy of asparagus officinalis. *Bot Gaz*. 1932;94:206–214.
37. Landuyt W, Ahmed B, Nuyts S, et al. In vivo antitumor effect of vascular targeting combined with either ionizing radiation or anti-angiogenesis treatment. *Int J Radiat Oncol Biol Phys*. 2001;49:443–450.
38. Tran L-B-A, Bol A, Labar D, et al. Potential role of hypoxia imaging using (18)F-FAZA PET to guide hypoxia-driven interventions (carbogen breathing or dose escalation) in radiation therapy. *Radiother Oncol*. 2014;113:204–209.
39. Caruso RA, Branca G, Fedele F, et al. Mechanisms of coagulative necrosis in malignant epithelial tumors (Review). *Oncol Lett*. 2014;8:1397–1402.
40. Neeman M, Freyer JP, Sillerud LO. A simple method for obtaining cross-term-free images for diffusion anisotropy studies in NMR microimaging. *Magn Reson Med*. 1991;21:138–143.
41. Manjon JV, Coupe P, Concha L, Buades A, Collins DL, Robles M. Diffusion weighted image denoising using overcomplete local PCA. *PLoS ONE*. 2013;8:e73021.
42. Coupé P. DWI denoising. https://sites.google.com/site/pierrickcoupe/softwares/denoising-for-medical-imaging/dwi-denoising. Accessed September 12, 2019.
43. Daducci A, Canales-Rodriguez EJ, Zhang H, Dyrby TB, Alexander DC, Thiran JP. Accelerated Microstructure Imaging via Convex Optimization (AMICO) from diffusion MRI data. *NeuroImage*. 2015;105:32–44.
44. Bonet-Carne E, Johnston E, Daducci A, et al. VERDICT-AMICO: ultrafast fitting algorithm for non-invasive prostate microstructure characterization. *NMR Biomed*. 2019;32:e4019.
45. Ozarslan E, Shemesh N, Basser PJ. A general framework to quantify the effect of restricted diffusion on the NMR signal with applications to double pulsed field gradient NMR experiments. *J Chem Phys*. 2009;130:104702.
46. Bar L, Sochen N. A spectral framework for NMR signal with restricted diffusion. *Concepts Magn Reson Part A Bridg Educ Res*. 2015;44:16–53.
47. Le Bihan D, Breton E, Lallemand D, Aubin ML, Vignaud J, Laval-Jeantet M. Separation of diffusion and perfusion in intravoxel incoherent motion MR imaging. *Radiology*. 1988;168:497–505.
48. Minati L, Węglarz WP. Physical foundations, models, and methods of diffusion magnetic resonance imaging of the brain: a review. *Concepts Magn Reson Part A Bridg Educ Res*. 2007;30A:278–307.
49. Benjamini D, Komlosh ME, Holtzclaw LA, Nevo U, Basser PJ. White matter microstructure from nonparametric axon diameter distribution mapping. *NeuroImage*. 2016;135:333–344.
50. Schneider C, Rasband W, Eliceiri K. NIH Image to ImageJ: 25 years of image analysis. *Nat Methods*. 2012;9:671–675.
51. Briguet A, Courdier-Fruh I, Foster M, Meier T, Magyar JP. Histological parameters for the quantitative assessment of muscular dystrophy in the mdx-mouse. *Neuromuscul Disord*. 2004;14:675–682.
52. White NS, Dale AM. Distinct effects of nuclear volume fraction and cell diameter on high b-value diffusion MRI contrast in tumors. *Magn Reson Med*. 2014;72:1435–1443.
53. Ozarslan E. Compartment shape anisotropy (CSA) revealed by double pulsed field gradient MR. *J Magn Reson*. 2009;199:56–67.
54. Lasič S, Oredsson S, Partridge SC, et al. Apparent exchange rate for breast cancer characterization. *NMR Biomed*. 2016;29:631–639.
55. Shepherd TM, Thelwall PE, Stanisz GJ, Blackband SJ. Aldehyde fixative solutions alter the water relaxation and diffusion properties of nervous tissue. *Magn Reson Med*. 2009;62:26–34.
56. Stylianopoulos T, Diop-Frimpong B, Munn LL, Jain RK. Diffusion anisotropy in collagen gels and tumors: the effect of fiber network orientation. *Biophys J*. 2010;99:3119–3128.
57. Li XY, Chen JQ, Xu YK, Han XJ. The relationship between fractional anisotropy value and tumor microarchitecture in late-stage rat glioma. *Asian Pac J Trop Med*. 2017;10:607–611.
58. Bailey C, Siow B, Panagiotaki E, et al. Microstructural models for diffusion MRI in breast cancer and surrounding stroma: an ex vivo study. *NMR Biomed*. 2017;30. https://doi.org/10.1002/nbm.3679.
59. Szczepankiewicz F, Lasič S, van Westen D, et al. Quantification of microscopic diffusion anisotropy disentangles effects of orientation dispersion from microstructure: applications in healthy volunteers and in brain tumors. *NeuroImage*. 2015;104:241–252.
60. Chen Q, Kang J, Fu C. The independence of and associations among apoptosis, autophagy, and necrosis. *Signal Transduct Target Ther*. 2018;3:18.
61. Reynaud O, Winters KV, Hoang DM, Wadghiri YZ, Novikov DS, Kim SG. Pulsed and oscillating gradient MRI for assessment of cell size and extracellular space (POMACE) in mouse gliomas. *NMR Biomed*. 2016;29:1350–1363.
62. Jespersen SN. Equivalence of double and single wave vector diffusion contrast at low diffusion weighting. *NMR Biomed*. 2012;25:813–818.

SUPPORTING INFORMATION

Additional supporting information may be found online in the Supporting Information section at the end of the article.

FIGURE S1 Results of simulations. A, Accuracies and precisions (mean difference with GTV ± 1 standard deviation) of DDE estimates in viable and necrotic synthetic tissues. B, Mean of estimated ROI value ± 1 SEOM in viable and necrotic synthetic tissues. C, Accuracies and precisions of DDE estimates for varying parameter values with SNR fixed to 100

How to cite this article: Duchêne G, Abarca-Quinones J, Leclercq I, Duprez T, Peeters F. Insights into tissue microstructure using a double diffusion encoding sequence on a clinical scanner: Validation and application to experimental tumor models. *Magn Reson Med*. 2019;00:1–14. https://doi.org/10.1002/mrm.28012